Title
Hydro-mechanical model for wetting/drying and fracture development in geomaterials

Authors
Asahina, D
Houseworth, JE
Birkholzer, JT
et al.

Publication Date
2014-04-01

DOI
10.1016/j.cageo.2013.12.009

Peer reviewed

Hydro-Mechanical Model for Wetting/Drying and Fracture Development in Geomaterials

D. Asahina[a], J. E. Houseworth[a], J. T. Birkholzer[a], J Rutqvist[a], and J. E. Bolander[b]

[a] *Earth Sciences Division, Lawrence Berkeley National Laboratory, One Cyclotron Rd, Berkeley, CA 94720, USA*

[b] *Department of Civil and Environmental Engineering, University of California, Davis, One Shields Avenue, Davis, CA 95616, USA*

Submitted for publication in Computers & Geosciences

Refer to final version published as:

Asahina D., Houseworth J.E., Birkholzer J.T., Rutqvist J., and Bolander J.E. Hydro-mechanical model for fracture development and fluid transport in geomaterials. Computers & Geosciences, 65, 13-23 (2014).

Abstract:

This paper presents a modeling approach for studying hydro-mechanical coupled processes, including fracture development, within geological formations. This is accomplished through the novel linking of two codes: TOUGH2, which is a widely used simulator of subsurface multiphase flow based on the finite volume method; and an implementation of the Rigid-Body-Spring Network (RBSN) method, which provides a discrete (lattice) representation of material elasticity and fracture development. The modeling approach is facilitated by a Voronoi-based discretization technique, capable of representing discrete fracture networks. The TOUGH-RBSN simulator is intended to predict fracture evolution, as well as mass transport through permeable media, under dynamically changing hydrologic and mechanical conditions. Numerical results are compared with those of two independent studies involving hydro-mechanical coupling: (1) numerical modeling of swelling stress development in bentonite; and (2) experimental study of desiccation cracking in a mining waste. The comparisons show good agreement with respect to moisture content, stress development with changes in pore pressure, and time to crack initiation. The observed relationship between material thickness and crack patterns (*e.g.*, mean spacing of cracks) is captured by the proposed modeling approach.

Key words: coupled modeling; TOUGH2; lattice models; discrete fracture network; desiccation cracking; Voronoi tessellation

1. Introduction

Geomechanical processes are known to play an important role in hydrogeological behavior (Neuzil, 2003; Rutqvist and Stephansson, 2003). Linkage between mechanics and hydrogeology occurs in two fundamental ways: (1) through interactions between rock strain, the geometry of pores and fractures, and their permeability and porosity; and (2) through interactions between fluid pressure and rock mechanical stress (Rutqvist and Stephansson, 2003). Although a number of numerical models have been developed using continuum approach for the analysis of hydro-mechanical behavior under single phase flow conditions (*e.g.*, Noorishad *et al*., 1982) and multiphase flow conditions (*e.g.*, Rutqvist *et al*., 2002), the modeling of hydro-mechanical coupling with mechanistic representation of damage and fracture initiation/propagation remains a major difficulty (Tang *et al*., 2002). Such processes are of particular importance for mechanically weak geomaterials such as clays and shales. As a further complication, fractures can exhibit transient behavior as a result of self-sealing processes (Bastiaens *et al*., 2007). Such issues are important, *e.g.*, for geo-environmental issues related to nuclear waste disposal (Bossart *et al*., 2004), geologic carbon sequestration (Chiaramonte *et al*., 2008), and hydraulic fracturing (Kim and Moridis, 2013).

Various numerical models have been developed to simulate the fracture behavior of geomaterials and structures. Such models can be broadly categorized, depending on whether the domain of interest is represented by continuum or discrete elements (Jing and Hudson, 2002). Discrete models are based on discontinuous approximations of the field variable over the computational domain, which facilitates the modeling of fracture and other discontinuous phenomena. This category includes lattice models, in which complex system behavior is represented by a collection of primitive two-node elements interconnected on a set of nodal points (Herrmann and Roux, 1990). Lattice models have been effective in studying the role of disorder in the fracture of a variety of materials, including concrete (van Mier, 1997). Particle-based methods, including the discrete element method (Cundall, 1971), are another means for studying the interactions of discrete features and their collective influence on the behavior of geological systems. Varieties of alternative approaches are also available, such as use of cellular automata (Pan *et al.*, 2012) or boundary element method (Shen *et al.*, 2004) to simulate fracture propagation in geomaterials. Although effective mechanical-damage models are available in the literature, the capabilities for simulating hydro-mechanical coupled processes, including fracture development, are still limited, especially for modeling fracture propagation in three dimensions.

Regarding fluid flow processes in the subsurface, discrete fracture network (DFN) models have been used for decades in situations where flow is dominated by a limited number of discrete pathways over the domain of interest, *e.g.*, in naturally fractured formations (Dershowitz *et al.*, 2004). DFN models successfully addressed shortcomings of conventional continuum methods that do not capture observed preferential transport along highly localized channels. The directional dependence of flow on fracture network geometry is particularly strong in sparsely fractured rock (Painter and Cvetkovic, 2005). Discrete fractures are typically represented in 3-D numerical models as planar regions or parallel-plane 3-D objects with high aspect ratios. In 2-D numerical models, fractures take the form of line segments or 2-D objects with high aspect ratios. DFN models have often been restricted to the representation of fracture flow paths, whereas transport within the low-permeable rock matrix is either ignored or represented by approximate methods. When the matrix volume needs to be represented explicitly, such as when mechanical processes are considered, the complex geometry of discrete fractures and matrix blocks can lead to difficulties in mesh generation, particularly in the presence of fracture connections at small angles and fractures with small interceding gaps (Paluszny *et al.*, 2007; Reichenberger *et al.*, 2006). Simple and reliable methods are needed to introduce potential fracture planes into the computational domain. Furthermore, some problem types require a dynamic representation of fracture development within the matrix and its coupling with fluid flow.

This paper presents a newly established linking of the finite volume method (*via* the TOUGH2 package (Pruess *et al.*, 2011)) and a lattice model based on the Rigid-Body-Spring Network (RBSN) concept (Kawai, 1978; Asahina *et al.*, 2011). TOUGH2 is used to simulate multiphase flow and transport through discrete fractures and within the matrix, whereas elasticity and fracture development are modeled by RBSN. The coupled analyses account for dynamically changing hydrologic-mechanical (HM) conditions that often exist in geological systems. Fractures are represented as discrete features that interact with a porous and permeable matrix. Existing or newly developed fracture configurations are mapped onto an unstructured, 3-D Voronoi tessellation of a spatially random set of points. One advantage of linking TOUGH2 and RBSN resides in their common utilization of a set of nodal points and properties of the corresponding Voronoi tessellation (*e.g.*, natural neighbor and volume rendering definitions). Shared use of the Voronoi tessellation facilitates every stage of the analyses, including model construction and results interpretation. Fractures propagate along Voronoi cell boundaries as HM-induced stresses evolve and exceed prescribed material strength values. After describing the methodology in Section 2, the basic capabilities of the modeling approach are demonstrated through two example applications: swelling stress development in bentonite (Section 3) and desiccation cracking in mining waste (Section 4).

2. Methodology

This section starts with brief reviews of the existing codes TOUGH2, for multi-phase flow and transport, and RBSN, for elasticity and fracture development of geomaterials (Sections 2.1 and 2.2). The linking between TOUGH and RSBN is described in Section 2.3. Several advantages of the coupled TOUGH-RBSN simulator stem from its use of Voronoi-based discretization techniques (Okabe *et al*., 2000), which allow discretization of dynamically changing DFNs with embedded matrix in a simple and straightforward manner. Although TOUGH2 has the capability to simulate temperature variations and some of their effects, the examples considered herein are limited to isothermal conditions.

2.1. Hydrological modeling: TOUGH2 simulator

TOUGH2 is a widely used general-purpose simulator for fluid flows of multiphase and multicomponent mixtures in porous and fractured materials (Pruess *et al*., 2011). The numerical solution scheme is based on the integral finite difference (or finite volume) method and is compatible with both regular and unstructured numerical grids. Simulations presented here use TOUGH2 with the equations of state (EOS) Module 4 for the hydrological processes of water flow and vapor diffusion. EOS Module 4 accommodates the transport of liquid water, water vapor, and air as a noncondensible ideal gas, and accounts for vapor-pressure-lowering effects (Pruess *et al*., 2011). For investigations involving hydro-mechanical continuum behavior, Rutqvist *et al*. (2002, 2011) have coupled TOUGH2 to a commercial mechanics simulator, FLAC3D (Itasca, 2009), which has been extensively used in geo-environmental applications.

As an integrated finite difference method, TOUGH allows for flexible gridding that can accommodate representation of fractures or fracture networks embedded in a porous permeable geomaterial (*e.g.*, Zhang *et al*., 2004; Rutqvist *et al*., 2013). Fractures may form, or partially form, an interconnected fracture network embedded within the matrix. By utilizing a discrete fracture approach, however, continuity of the fracture network is not assumed but rather explicitly modeled. Flow within fractures is generally assumed to follow Darcy's law. The intrinsic permeability assigned to individual fractures is often based on a parallel-plate model (Bear, 1972).

2.2. Mechanical-damage model: Rigid-Body-Spring Networks

2.2.1 Model formulation

Elasticity and fracturing of the permeable medium are modeled using the RBSN method (Kawai, 1978; Bolander and Saito, 1998), which can be viewed as a type of lattice model. Lattice topology is defined by the Delaunay tessellation of the nodal points within the computational domain. The basic unit of the RBSN is a 1-D lattice element (Fig. 1) that consists of: (1) a zero-size spring set located at the centroid of the Voronoi facet common to nodes *i* and *j*; and (2) rigid-arm constraints that link the spring set and the nodal degrees of freedom. Each node has six degrees of freedom for the 3-D case. The spring set is formed from three axial springs and three rotational springs (referenced to local coordinate axes *n*-*s*-*t*), as shown in Fig. 1, where the rotational springs have been omitted for clarity. The axial spring stiffnesses scale in proportion to A_{ij}/h_{ij}, where A_{ij} is the Voronoi facet area associated with nodes i and j, and h_{ij} is the distance between the same nodes. The spring stiffnesses are

$$k_s = k_t = \beta_1 k_n = \beta_1 \beta_2 E \frac{A_{ij}}{h_{ij}}, k_{\phi n} = E \frac{J_p}{h_{ij}}, k_{\phi s} = E \frac{I_{ss}}{h_{ij}}, k_{\phi t} = E \frac{I_{tt}}{h_{ij}} \quad (1)$$

in which E is the Young's modulus, subscript ϕ signifies the rotational spring terms, J_p, I_{ss}, and I_{tt} are the polar and two principal moments of inertia of the Voronoi facet area with respect to the facet centroid, respectively. By adjusting β_1 and β_2 in accordance with experimental results, macroscopic modeling of both elastic constants (E and Poisson's ratio, v) is possible. For the special case of $\beta_1 = \beta_2 = 1$ (which was used for the simulations presented herein), the RBSN is elastically homogeneous under uniform modes of straining, albeit without proper modeling of the Poisson effect (Bolander and Saito, 1998; Asahina *et al*., 2011). The six spring coefficients are placed in a diagonal matrix

$$D = (1-\omega)\, diag[k_n, k_s, k_t, k_{\phi n}, k_{\phi s}, k_{\phi t}] \quad (2)$$

from which the element stiffness matrix can be formed. Here, ω is a damage index that ranges from 0 (undamaged) to 1 (completely damaged). Despite the unusual configuration of a RBSN element (Fig. 1), its stiffness matrix is akin to that of an ordinary frame element. Element matrices are assembled to form the system equilibrium equations in the conventional manner.

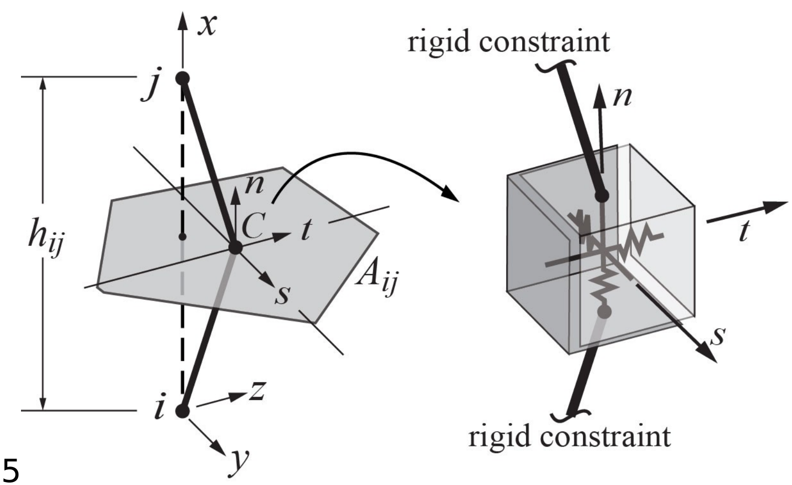

Fig. 1. Typical lattice element *ij* with a zero-size spring set located at centroid *C* of facet area A_{ij}. Note that A_{ij} is the Voronoi facet or cell boundary, and *i* and *j* are the neighboring Voronoi cell nodes (matrix nodes).

2.2.2 Fracture model

A fracture is represented by the controlled breakage of the springs linking adjacent Voronoi cells along the fracture trajectory. Forces and/or displacements are applied incrementally with equilibrium iterations in each increment. Only one element is allowed to break per iteration. For each element *e* within the model, a stress ratio can be expressed by

$$\rho_e = \sigma_e / \hat{\sigma} \tag{3}$$

where σ_e is a measure of stress within element *e* and $\hat{\sigma}$ is the material strength. The most critical element with the highest $\rho_e>1$ undergoes fracturing, which entails a reduction of its elastic stiffness and an associated release of element forces. In general, loading direction seldom coincides with the element axis *ij* and, therefore, both the normal and tangential springs are typically activated. The resultant of the set of forces in the axial springs, $F_R= (F_n^2+ F_s^2+ F_t^2)^{0.5}$, is used to obtain a measure of tensile stress within each element

$$\sigma_R = F_R / A_{ij}^P \tag{4}$$

where A_{ij}^P is the projected area of A_{ij} on a plane perpendicular to F_R. This σ_R serves as σ_e in Eq. (3), whereas $\hat{\sigma}$ varies according to a prescribed tensile softening relation. This representation of fracturing within the RBSN is energy conserving and mesh insensitive for predominantly tensile stress fields, *i.e.*, fracture propagates through the random mesh with uniform, controllable energy consumption, as if using a straight-line discretization of the crack trajectory (Bolander and Sukumar, 2005; Berton and Bolander, 2006). As shown in Fig. 2, tensile softening of the RBSN approaches the traction-free condition naturally, without the stress locking and artificial energy consumption that is often associated with fracturing of continuum finite elements. Similar approaches have been used to simulate interface failure in multiphase composites (Yip *et al*., 2006), fracturing under multiaxial stress conditions (Asahina *et al*., 2011), shear banding in compression, and other difficult modeling problems such as fracturing and damage of concrete (Cusatis *et al*., 2003; Nagai *et al*., 2005; Cusatis *et al*., 2011).

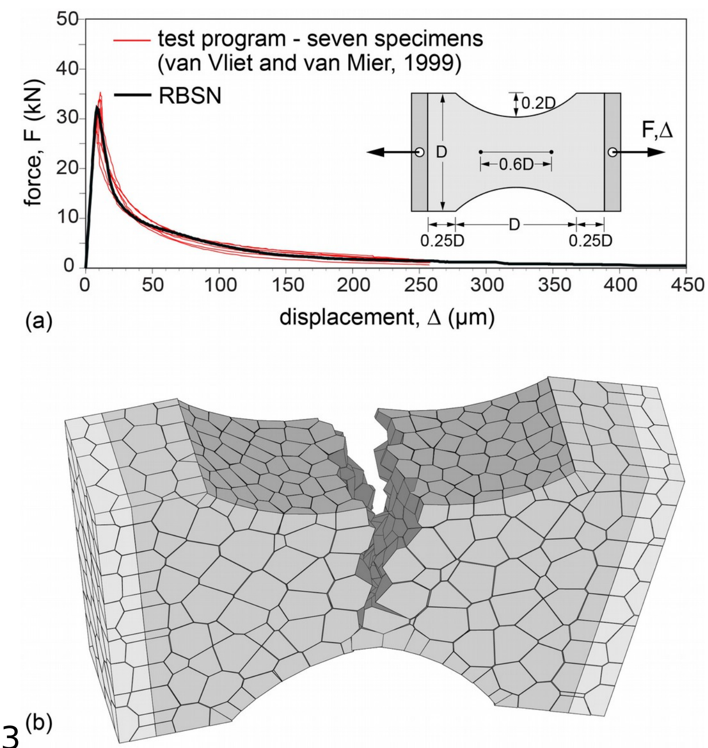

Fig. 2. Uniaxial tension test of concrete: a) load-displacement results; and b) crack propagation simulated by RBSN. (Adapted from Sukumar and Bolander, 2013)

2.3. Coupling of hydraulic and mechanical damage codes

Rutqvist *et al*. (2002) have coupled TOUGH2 to a commercial continuum-mechanics simulator, FLAC3D. The general procedure for coupling TOUGH2 and RBSN is similar, but substantially modified and extended for modeling discrete fracture propagation. Figure 3 shows a schematic flowchart of the linking process between TOUGH2 and RBSN. In this paper, TOUGH2 is used to simulate the scalar quantities (*e.g.*, pressure and degree of saturation) associated with fluid flow, whereas RBSN accounts for the mechanical quantities (*e.g.*, displacement, strain, and stress) of interest. Such primary variables are coupled through simplified linear relationships or through nonlinear empirical expressions, which could be estimated by laboratory experiments with appropriate calibration. As previously noted, an advantage of coupling TOUGH2 and RBSN is that both models share the same unstructured, 3-D Voronoi grid and the same set of nodes, which simplifies their data exchange. TOUGH2 and RBSN are currently linked through an external module, which handles two-way transfer of the relevant quantities at each time step. First, a TOUGH2 to RBSN link supplies multiphase pressure and degree of saturation to update the mechanical quantities. The conventional effective stress law of Biot's theory for a fully saturated media is (Biot and Willis, 1957)

$$\sigma = \sigma' - \alpha_p P I \tag{5}$$

where σ is the total stress tensor, σ' is the effective stress tensor, α_p is the Biot effective stress parameter, P is the pore pressure, and I is the identity tensor. Note that tensile stress is positive. The example application presented in Section 3 assumes pore pressure to be the maximum of the gas or liquid phase pressures

$$P = max(P_g, P_l) \tag{6}$$

where P_g is gas pressure and P_l is liquid water pressure (Rutqvist et al., 2001; Vilarrasa et al., 2010). This approach is used for both saturated and unsaturated conditions. For example, under single phase conditions, the first primary variable is P_g or P_l. For two phase conditions, the primary variable is gas pressure, which is generally greater than the liquid pressure. An alternative way to represent pore pressure is by taking the volume average for the two phases

$$P = S_l P_l + (1 - S_l) P_g \tag{7}$$

where S_l is liquid phase saturation. A modified effective stress can be obtained by replacing S_l with Bishop's factor:

$$\sigma = \sigma' - \left[\chi(S) P_l + (1 - \chi(S)) P_g\right] I \tag{8}$$

where χ is Bishop's parameter, a function of the degree of saturation, which was measured experimentally for several geomaterials (Bishop et al., 1960). The choice of the definition of pore pressure is problem specific and depends on the target materials. In incremental form, Eq. (5) becomes

$$\Delta\sigma_n = \Delta\sigma_n' - \alpha_p (\Delta P_i + \Delta P_j)/2 \tag{9}$$

where σ_n is the stress normal to lattice element *ij*, and ΔP_i and ΔP_j are the changes in pore pressures over the time step at neighboring nodes *i* and *j*. Note that the pore pressure only affects the spring in the normal direction. It is assumed that the local changes of liquid saturation induce strain as follows:

$$\Delta \varepsilon_s = \alpha_s (\Delta S_i + \Delta S_j)/2 \tag{10}$$

where ε_s is shrinkage/swelling strain; ΔS is the change in saturation over the time step in one lattice element; and α_s is the hydraulic shrinkage coefficient. ΔS is taken as the average of two neighboring nodes *i* and *j*. For an expansive soil material, the effective stress can be affected by swelling/shrinking strain as

$$\Delta \sigma'_n = \Delta \varepsilon_s E \tag{11}$$

Thereafter, a RBSN to TOUGH2 link supplies the stress and strain values from the lattice elements to update the hydrogeological property values associated with each Voronoi cell in the TOUGH2 model (Fig. 3). The following general relations are considered (Rutqvist and Tsang, 2002)

$$\phi = \phi(\sigma', \varepsilon) \tag{12}$$

$$K = K(\sigma', \varepsilon) \tag{13}$$

$$P_c = P_c(\sigma', \varepsilon) \tag{14}$$

where ϕ is porosity, K is permeability, and P_c is capillary pressure. The permeability of an individual fracture depends on its aperture, *b*. Herein, a parallel-plate model is used in which permeability is set equal to $b^2/12$ (Bear, 1972). The example applications presented later (in Sections 3 and 4) demonstrate the coupling shown on the left side of Fig. 3 (*i.e.*, the use of pressure and degree of saturation supplied by TOUGH2 to drive the mechanical-damage model). A subsequent paper will demonstrate capabilities for two-way coupling of thermal-hydrologic-mechanical (THM) processes, including abilities to simulate crack-assisted mass transport.

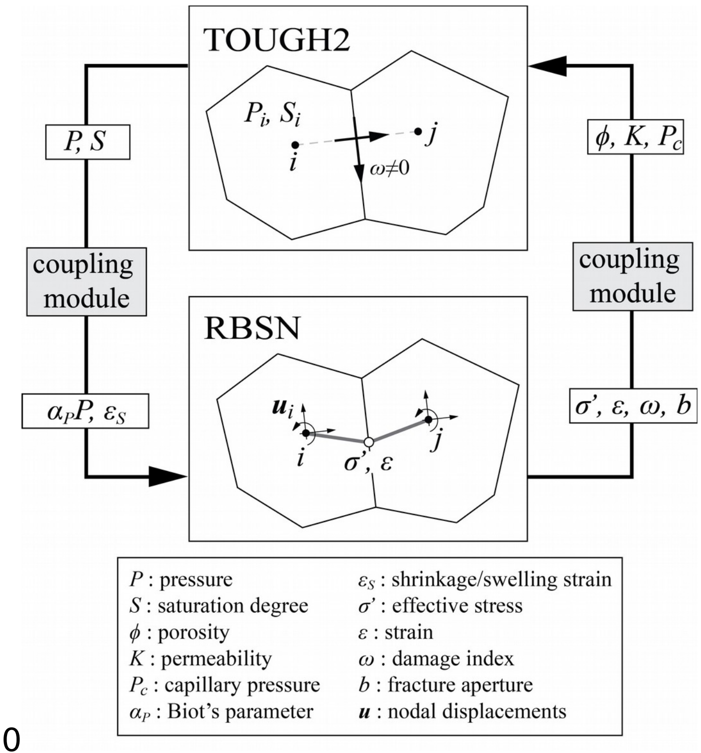

Fig. 3. Flow diagram of TOUGH2-RBSN linkages for a coupled hydrologic-mechanical (HM) simulation. Note that additional nodes and connections are introduced in TOUGH2 to activate flow pathways associated with fracture.

2.4. Model construction

2.4.1 Voronoi discretization

To represent discrete fractures in a permeable porous geomaterial, the computational domain for both TOUGH2 and RSBN is effectively discretized as the Voronoi tessellation (Okabe *et al.*, 2000) of an unstructured set of nodal points. In this study, nodal points are sequentially placed into the domain using a pseudo-random number generator. The use of a random point set simplifies mesh generation and avoids potential bias on fracture patterns associated with regular point sets. A minimum allowable distance l_m between nodes is prescribed to control the nodal point density. With continued nodal point insertion, under the l_m constraint, the domain is eventually saturated with nodes (Asahina and Bolander, 2011). The Delaunay tessellation of the nodal points defines their connectivity. The dual Voronoi tessellation serves to partition the spatial domain and define model properties, as described in Section 2.2.1.

2.4.2. Discrete fracture representation

A fracture is considered to be a discrete feature that facilitates flow and mass transport. The model explicitly represents such crack-assisted flow and its coupling to flow within the permeable medium. Existing or newly generated fractures are directly mapped onto the Voronoi grid representing the spatial domain of the system. Figure 4a shows a reference fracture and its approximation by a series of Voronoi cell boundaries. Descriptors of the fracture geometry can be obtained by field mapping, computer-generated statistical representations, or the simulation outcomes of mechanical models. With reference to the 2-D case, a straight-line fracture is discretized as follows (Fig. 4a):

- Discretize the spatial domain with an irregular Voronoi grid.
- Overlay the reference fracture onto the Voronoi grid.
- Select node-node (natural neighbor) connections that cross the reference fracture. The corresponding Voronoi cell boundaries of such nodal connections represent the reference fracture.

By repeating this process, a network of reference fracture lines can be discretized. Figure 4b shows two intersecting fractures that are represented using different discretization strategies. Case 1 has been discretized as described above. The grid size should be selected to obtain a sufficiently accurate representation of the fracture line. As the nodal point density increases, the discretized path more closely resembles a line. Advantages of this DFN generation approach include the abilities to: (1) simply activate and connect new discrete fractures; (2) automatically handle discrete fracture intersections; (3) control mesh gradation (nodal density), which can be advantageous for reducing computational expense; and (4) straightforwardly extend to more complicated 3-D geometries.

Alternatively, straight-line fractures can be precisely discretized, as shown by Case 2 in Fig. 4b, through strategic placement of nodal pairs prior to introducing the random nodal point set. Nodes in each pair are equidistant from, and aligned normal to, the fracture line. Such DFN discretization, however, is either cumbersome or intractable due to difficulties in placing nodal points to define intersections of planar fractures, especially for inclined fracture intersections in 3-D.

By automating the process of the proposed DFN approach, fracture intersections in 3-D can be effectively generated. Figure 4c presents the 3-D version of the Voronoi grid of Fig. 4b, where the fractures have been opened to show internal grid structure. Visualization of the DFN is straightforward, since it simply involves plotting the Voronoi facets that tile the fracture surfaces. The mapping of material features onto a computational grid has been used in the modeling of multiphase composite materials such as concrete (van Mier, 1997). Heterogeneous features of the phase boundaries can be represented through the probabilistic assignment of interface element properties (Asahina *et al*., 2011).

It is possible to activate dynamically forming flow pathways along a discrete fracture, in which fracture nodes and associated connections are introduced at the Voronoi cell boundary. This additional kind of hydro-mechanical coupling will be demonstrated in a subsequent paper.

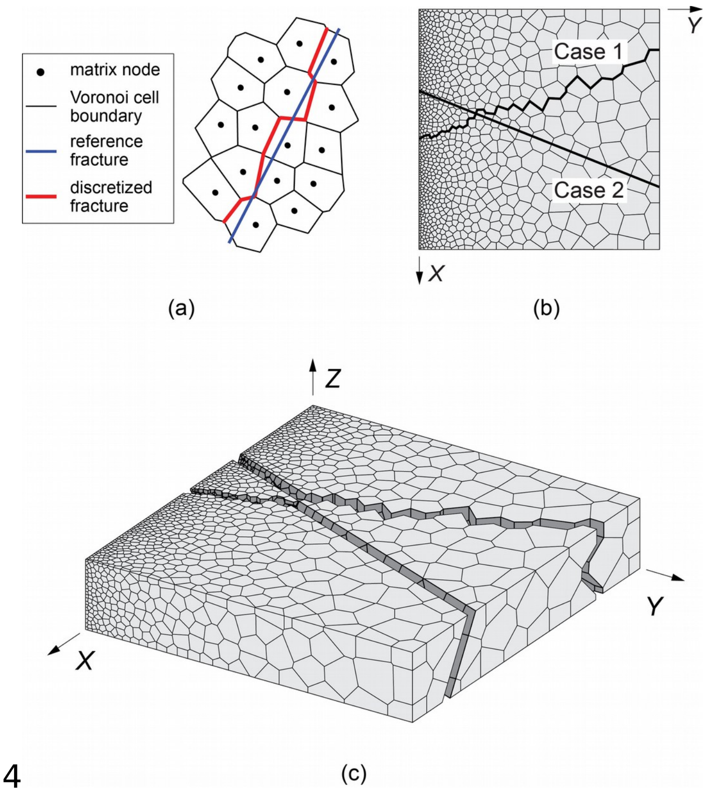

Fig. 4. (a) Mapping of a fracture geometry onto an irregular Voronoi grid, (b) two intersecting discretized fractures within a graded Voronoi grid; and (c) 3-D representation with open fractures.

3. Swelling test simulation

The first application example of the TOUGH-RBSN simulator features a comparison with an independent simulation of hydromechanical continuum processes using TOUGH-FLAC (Rutqvist *et al*., 2011). As mentioned above, the TOUGH-FLAC simulator is a continuum-based code with the capability to simulate coupled THM processes under multiphase fluid flow conditions. The example given here is based on experimental data that were a part of an international model comparison project on nuclear waste repositories, DECOVALEX III (Alonso *et al*., 2005). A bentonite with a dry-density of 1.6 g/cm^3 was used as a test material.

Consider a soil sample (20×20×20 mm) that is wetted at the bottom and fully confined mechanically, as shown schematically by the inset in Fig. 5. The model is discretized with 20 nodes and 19 lattice elements. Model boundaries are fully confined with mechanically fixed supports, and no flow is permitted across the boundaries except at the wetting surface at the bottom. The Young's modulus is set to 18 MPa, which was assigned as an average representative value for this bentonite (Rutqvist et al., 2011). As per test conditions, the initial degree of saturation is 65%, and the sample is fully saturated at the end of the test. The porosity and permeability is set to 0.389 and 2.0×10^{-21} m^2, respectively. A target compressive swelling stress of 5 MPa was to be induced by the saturation changes. From this information, the hydraulic shrinkage coefficient, α_s, which can be back-calculated using Eqs. (10) and (11), was found to be 0.794. Water is infiltrated from the bottom by fixing the bottom boundary at full saturation and at a gas pressure of 0.5 MPa. Moreover, the initial gas pressure within the sample was set to 0.1 MPa, whereas the initial (isotropic) stress was set slightly higher to 0.12 MPa. The simulation was conducted for about 10 days at isothermal conditions (T=25°C).

Figure 5 shows the TOUGH2 simulation results for gas pressure and saturation with time at point P1 within the swelling model. The simulation results accurately represent those reported in Rutqvist *et al*. (2011), in which the sample becomes fully saturated in 9 days and a temporal over pressure occurs as a results of trapped air in the upper part of the simulated sample. Figure 6 shows the computed values of compressive stress with time. The final stress without the effect of gas pressure is 5.12 MPa, which consists of 5 MPa (the calibrated value for stress caused by saturation change) on top of the initial stress of 0.12 MPa. The effect of gas pressure can be observed by changing the Biot's parameter, α_p (Fig. 6). The TOUGH-RBSN and TOUGH-FLAC simulation results agree well.

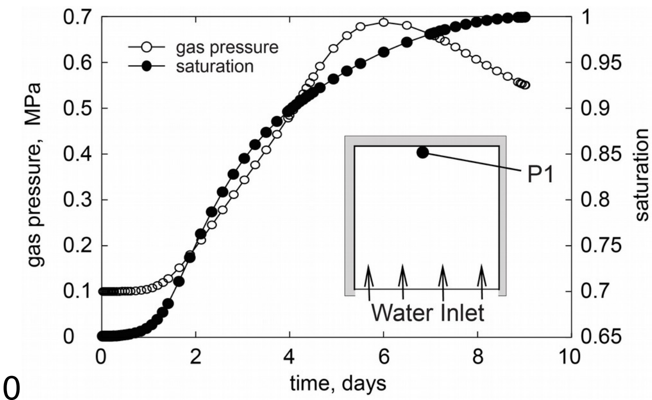

Fig. 5. TOUGH2 simulation of saturation and gas pressure with time at point P1 within the swelling model.

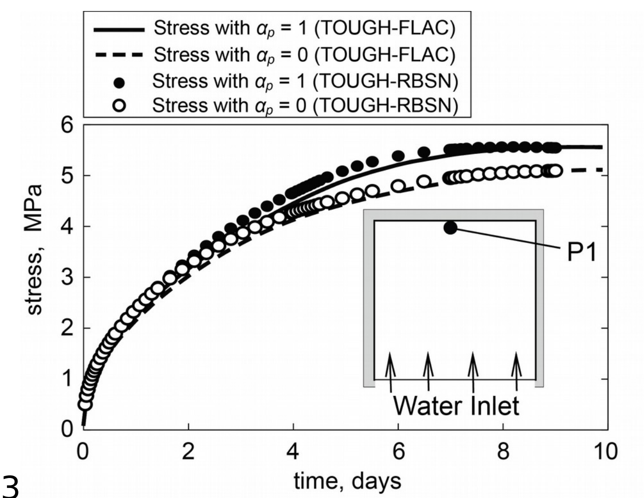

Fig. 6. Simulated time evolution of compressive stress at point P1 for simple swelling models.

4. Simulation of desiccation cracking of a mining waste

The second example involves desiccation cracking in a geomaterial. Here, the TOUGH-RBSN simulator is used to demonstrate the capability of modeling hydromechanically-induced fracturing. Desiccation can occur due to loss of moisture through an exposed surface, which induces differential straining within the material volume. Differential straining, and straining under restraint, can produce tensile stresses of sufficient magnitude to initiate cracking. Desiccation cracking of clay has been the subject of many experimental studies (Konrad and Ayad, 1997; Colina and Roux, 2000; Lakshmikantha *et al*., 2012). Numerical models have also been developed to study desiccation cracking (Amarasiri *et al*., 2011; Kitsunezaki, 2011; Shin and Santamarina, 2011; Trabelsi *et al*., 2011). Numerical results given in this section are compared with the test results of Rodríguez *et al*. (2007), obtained from desiccation of a mining waste material. For several sample thicknesses, comparisons are made for shrinkage strain, moisture content, fracture pattern, mean spacing of cracks, and time to crack initiation.

4.1 Experimental program of Rodríguez *et al*. (2007)

The basic framework of the experimental program of Rodríguez *et al*. (2007) is briefly described here for completeness. Desiccation processes and associated crack patterns were studied with thin disk specimens of a mining waste. The main component of the waste is hematite, which mainly consists of fine particles (mostly particles smaller than 80 μm) and classified as low plasticity silt. The waste sample was placed in a circular plate with only the top surface exposed to atmospheric desiccation, and with the inside bottom of each plate grooved to prevent sliding between the plate and the waste. Rodríguez *et al*. (2007) performed two sets of drying experiments, in which samples were (1) exposed to ambient conditions, or (2) dried in hermetically closed containers. In this study, we focus on the latter set of experiments, due to the better control of temperature and air movement near the material surface. Table 1 summarizes the material properties measured on samples before the drying test. Figure 7 shows the dependencies of elastic modulus and tensile strength on degree of saturation, which were obtained from a series of experiments. The material was fully saturated at the start of the test. Gravimetric moisture contents (Fig. 8) and vertical strain at the top surface were measured during exposure to the drying environment. Other measurements related to cracking behavior (*i.e.*, time to crack initiation, mean spacing of cracks, moisture contents and vertical strain at the moment of crack initiation) are given in Table 2. As Rodríguez *et al*. (2007) discuss in their conclusions, the experimental study showed the clear influence of sample thickness on distance between cracks. Such experimental observation has also been reported in the literature (Colina and Roux, 2000; Lakshmikantha *et al*., 2012).

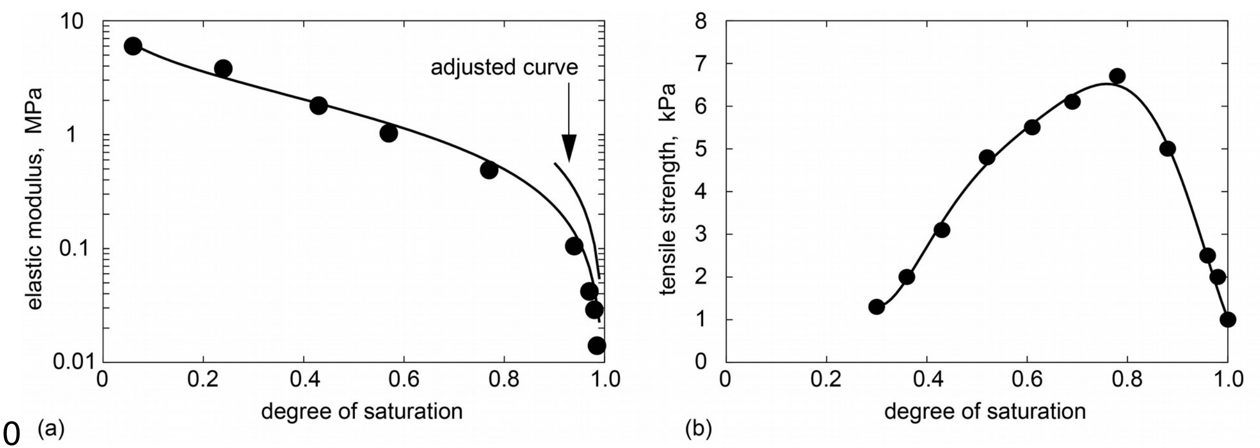

Fig. 7. Experimental data (after Rodríguez *et al*., 2007) and fitted polynomial curves of: (a) Young's modulus, and (b) tensile strength with degree of saturation.

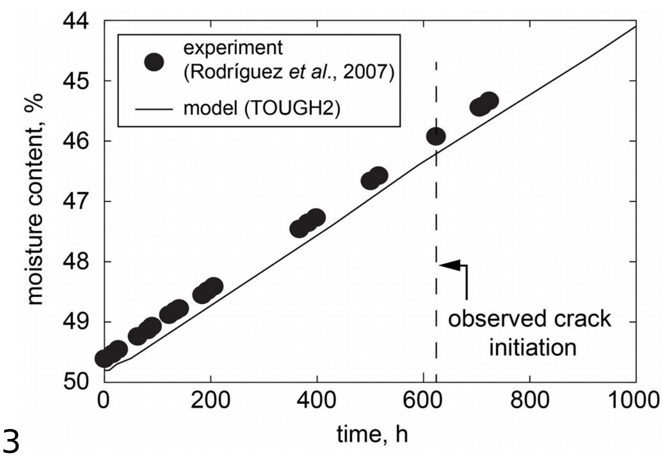

Fig. 8. Evolution of gravimetric moisture content of sample with thickness of 16mm.

405

43
44

Table 1. Summary of material properties of the mining waste used for TOUGH-RBS

4.2 Model description

Consider the 3-D model shown in Fig. 9, which represents the mining waste sample subjected to drying from the top surface. As indicated in Table 2, samples 225 mm in diameter with three different thicknesses (4 mm, 8 mm, and 16 mm) are considered as in the experimental program. For thinner specimens, a smaller nodal spacing is used to resolve the thickness direction. Although the crack patterns of similar desiccation tests have exhibited an effect of lateral dimension as well as thickness (Colina and Acker, 2000; Bisschop, 2008), the effect of specimen lateral dimensions is less significant than that of its thickness.

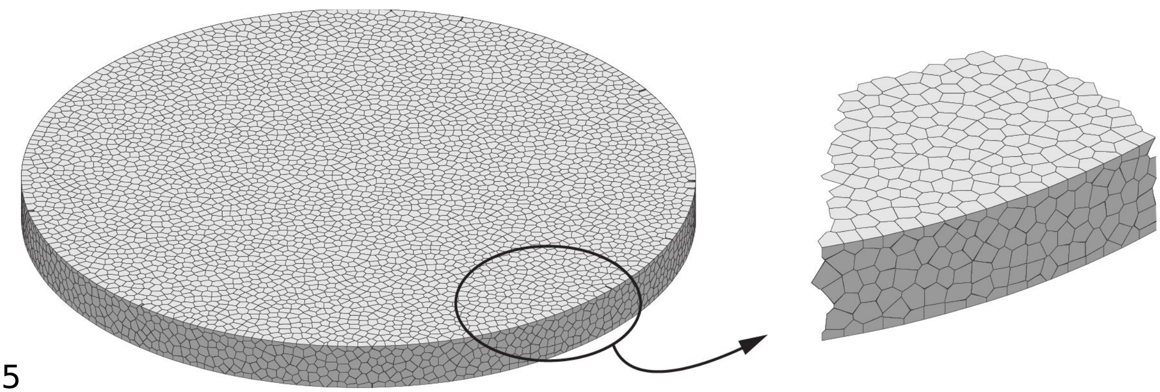

Fig. 9. Voronoi discretization of the mining waste sample with 16 mm thickness.

TOUGH2 models flow of both gas and liquid phases in response to their respective pressure (or concentration) gradients. Prior to drying, the matrix is initially saturated with water; as water evaporates, a capillary pressure gradient develops, causing water movement in the matrix toward the drying surface. The hydraulic boundary condition at the top of the specimen is implemented by prescribing a constant value of the relative humidity of environment, 75.7%, for a node representing a large volume above the top surface. The air partial pressure in Table 1 is obtained from saturated vapor pressure at constant temperature, 22.0°C, and the relative humidity of the environment. Hydraulic connections are made to the surface nodes, but there are no connections to the mechanical model. The distance between the desiccant and the top of the sample was set using a diffusive resistance length to represent water vapor diffusion as described by Ghezzehei *et al*. (2004). The diffusive resistance length, δ , is related to the steady-state diffusive mass flux by

$$J_v = D_v \frac{C^0 - C^\infty}{\delta} \tag{15}$$

where J_v is the steady-state diffusive mass flux between constant humidity boundaries at the soil surface, C^0 , and at the desiccant, C^∞ , and D_v is the vapor diffusion coefficient. The vapor mass flux was computed using TOUGH2 with the EOS7R equation of state module (Oldenburg and Pruess, 1995). The model grid represented the desiccator diffusion path geometry as used in the Rodríguez *et al*. (2007) experiments. The value of D_v used was 2.83×10^{-5} m^2/s. The specific value of $C^0 - C^\infty$ is not important since J_v is proportional to $C^0 - C^\infty$; $C^0 - C^\infty$ is set to the same value used to calculated J_v . The steady-state diffusive flux was determined from the TOUGH2 calculation to be 7.64×10^{-7} kg/m^2-s, giving a diffusive resistance length of 0.37 m.

For mechanical boundary conditions, the bottom layer of nodes (0.1 mm above the bottom surface) is restrained, whereas others are free to move. The mechanical bond between the sides of the plate mold and the waste material is considered to be negligible. In these analyses, neither external mechanical loading nor gravitational loading is considered.

Two parameters (sample thickness and nodal density) are varied, whereas the other input parameters are kept constant. Material properties are taken directly from the experimental measurements of Rodríguez *et al*. (2007), as presented in Table 1 and Fig. 7. The van Genuchten function is used to describe the water-retention characteristic curves (van Genuchten, 1980):

$$P_c = -P_0 \left[\left(\frac{S_l - S_{lr}}{S_{ls} - S_{lr}} \right)^{\frac{-1}{\lambda}} - 1 \right]^{1-\lambda} \qquad (16)$$

where P_0 is the air entry pressure, S_l is water saturation, the subscripts l_s and l_r refer to the fully saturated and residual conditions, respectively, and λ is a material parameter. Table 1 presents these values. In Fig. 7, curves were fit to the experimental measurements of elastic modulus and tensile strength versus the degree of saturation. We used results from the 16 mm sample to calibrate the elastic modulus, and then performed blind forward modeling for the 4 mm and 8 mm samples to demonstrate predictability. Accurate representation of time to initial cracking of the 16 mm sample (Fig. 8) was achieved by increasing the elastic modulus by a factor of 2.4 for degrees of saturation ranging from 0.9 to 1.0. Adjustment was made to the elastic modulus, rather than to other parameters, since few data points were provided in that region of rapid change.

Evaporation (or condensation) of water occurs at all gas-liquid interfaces, both inside the matrix and at the top surface, however, mass transport through the mining waste matrix is dominated by capillary flow whereas evaporation is the only mechanism that permits H_2O to exit the matrix at the top surface. Fractures induced by shrinkage stress are not coupled into the hydrologic model for this calculation. Therefore, fluid movement and vapor diffusion through fractures are not included. This is not considered a serious omission, however, because the limiting rate for fluid movement overall is vapor diffusion from the top of the matrix. In this section, TOUGH and RBSN are coupled only through Eq.(10). The hydraulic shrinkage coefficient, α_s (Eq.(10)), is determined from the ratio of the saturation change to strain change up to the moment of crack initiation observed in the 16 mm sample. Based on the value of moisture contents in Fig. 8, and other hydraulic variables (*i.e.* porosity, initial dry density), saturation at the moment of crack initiation can be calculated as 92.4%. With the average vertical strain of 2.72%, the coefficient, α_s, can be determined as 0.358 according to Eq.(10).

Drying shrinkage produces tensile stresses in the mining waste, which leads to of the formation of fractures in the RBSN model. The simulations were conducted until no significant changes occurred in the crack patterns. Other complex mechanisms associated with wetting and drying cycles, time-dependent repetitive crack growth, and crack-assisted mass transport are not included in this simulation. Furthermore, material aging and creep have not been modeled in the simulation presented here because short test durations have been considered. Such factors are being considered for extending the applicability of the simulation tools to broader classes of problems.

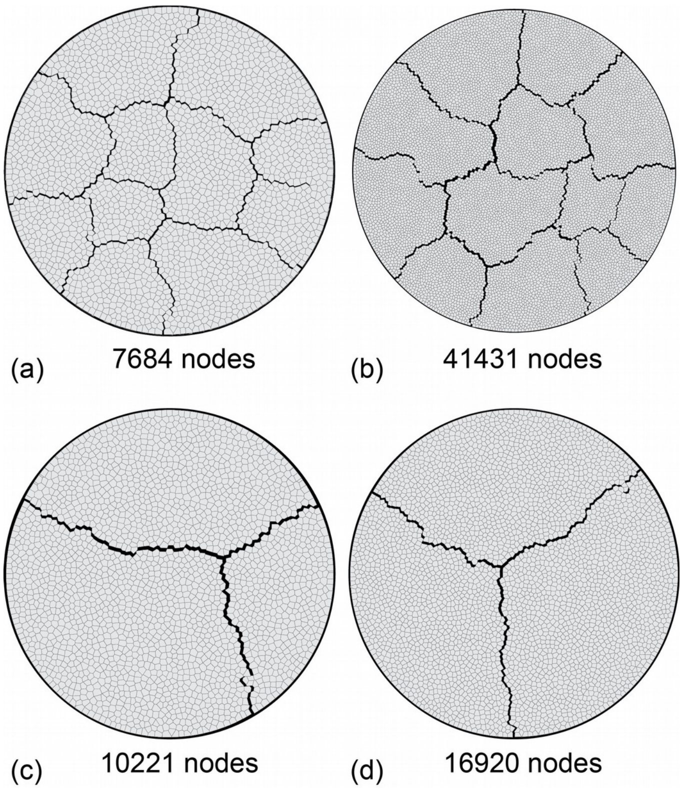

Fig. 10. Dependence of crack patterns on nodal density for sample thicknesses of: (a), (b) 8 mm; and (c), (d) 16 mm.

4.3 Simulation results

Sensitivity of the fracture pattern with respect to mesh size was studied using different nodal densities for sample thicknesses of 8 and 16 mm (Fig. 10). To make quantitative comparisons between the crack patterns, the mean spacing of cracks is measured according to Colina and Roux (2000). For the comparisons presented in Fig. 10, the mean crack spacings are: 47.2 and 51.9 mm for results (a) and (b), and 98.8 and 101.3 mm for results (c) and (d), respectively. In lieu of more rigorous studies of mesh sensitivity, these results provide assurance that crack patterns are sufficiently independent of nodal density (for the purpose of demonstrating model capabilities through the examples that follow).

Table 2 presents simulated results for each sample thickness. As expected, the time to crack initiation agrees with the test results for the 16 mm specimen. The results for the other specimens (*i.e.*, those with thicknesses of 4 and 8 mm), which can be viewed as predictions, are not as accurate as the 16 mm results, but show good qualitative agreement with slight underestimation of initiative time. The saturation ratio, obtained from the gravimetric moisture contents, is the average value for all nodes. The following observations can be made and agree with the concluding remarks of Rodríguez *et al*. (2007):

- The time of crack initiation is roughly proportional to the sample thickness.
- The vertical strain at the moment of crack initiation does not appear to be affected by the sample thickness.
- The mean spacing of cracks increases with the sample thickness.

Figure 11 shows the crack patterns of the samples listed in Table 2. Cracks are connected and appear to bound islands of material when viewed in plan. Also, the cracks tend to meet at triple junctions in both the test results and numerical simulations. Agreement between the numerical and physical test results (with respect to time to initial cracking, trends in mean crack spacing, and qualitative representation of the crack patterns) is quite good, especially considering the strong dependence of elastic modulus and tensile strength on degree of saturation. The strain gradient, produced by drying from the free surface, is affected by the transport properties of the medium and restraint conditions. Due to restraint between the sample and base plate, the shallower samples exhibit larger strain gradients and, thus, propensity for cracking (Fig. 12). Groisman and Kaplan (1994) and Shorlin et al. (2000) have described similar proportionality between crack spacing and sample depth, with the constant of proportionality being larger for reduced friction between the material layer and the substrate.

Although the numerical results capture the general trend between mean crack spacing and sample thickness (Fig. 12), the numerical results overestimate the crack spacings. This discrepancy is possibly due to toughening behavior of the mining waste, which was not considered in these simulations. Lakshmikantha *et al*. (2012) discuss the importance of fracture toughness when studying the mechanisms of desiccation cracking. Residual stress transfer across forming cracks would promote additional cracking.

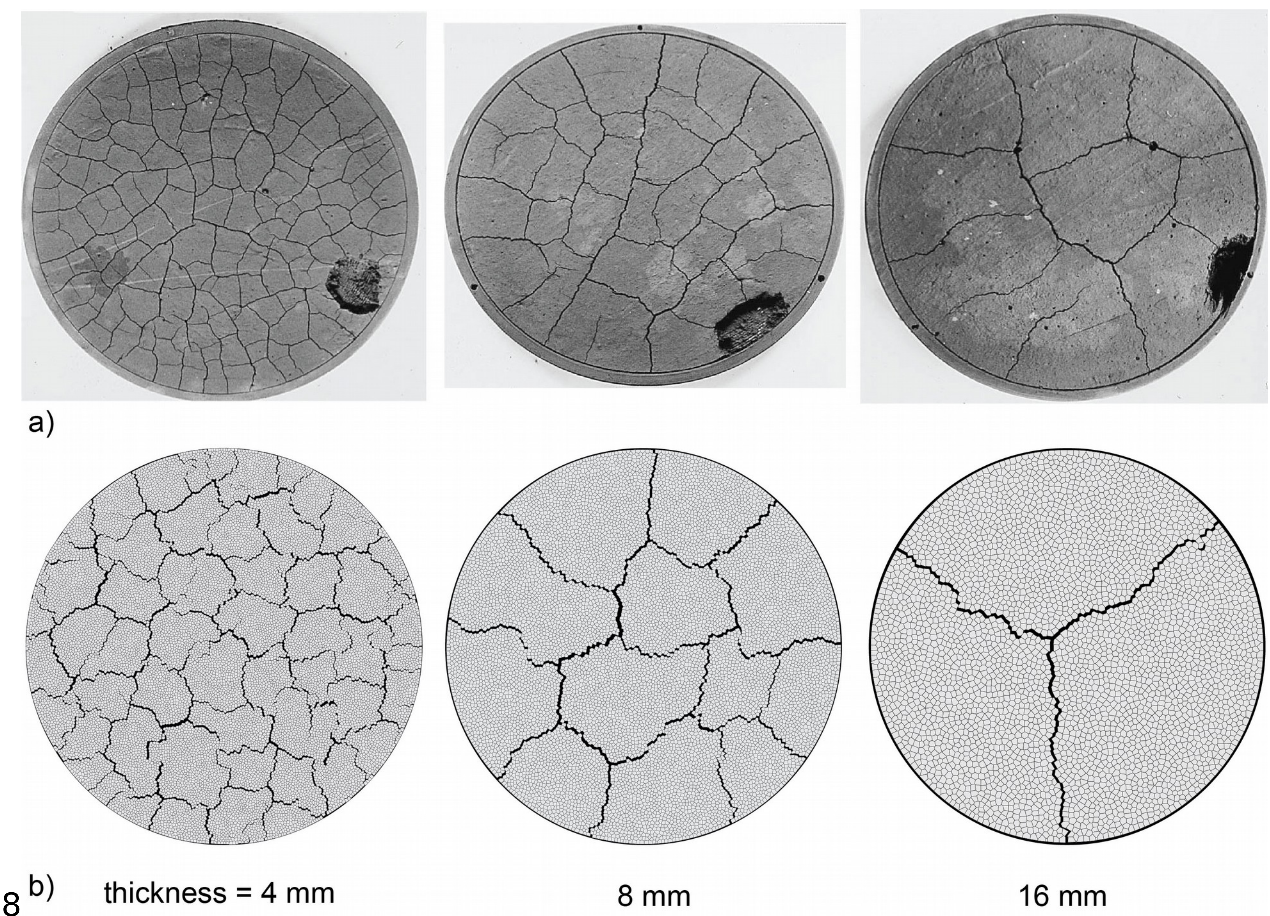

Fig. 11. Crack patterns for different sample thicknesses: (a) experimental results of Rodríguez *et al*. (2007), and (b) plan view of 3-D simulation results of the TOUGH-RBSN simulator.

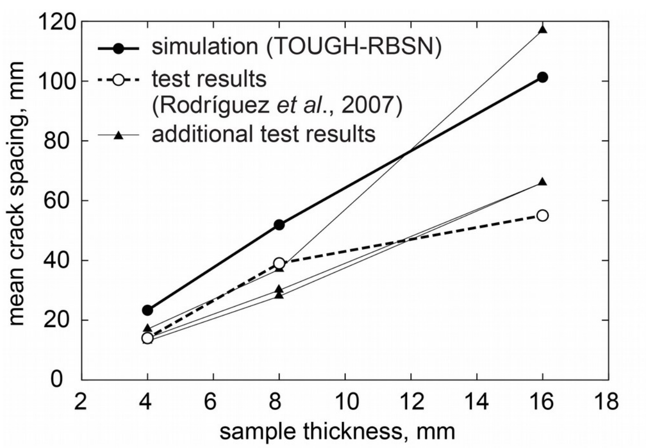

Fig. 12. Variation of mean spacing of cracks with sample thickness. The additional test results are also taken from Rodríguez *et al*. (2007), but for different drying conditions.

5. Conclusion

We have established an effective linking of two numerical methods: the finite volume method (*via* the TOUGH2 package) to simulate mass transport within a permeable medium; and the RBSN method, which provides a discrete representation of material elasticity and fracture development in three dimensions. One main advantage of linking TOUGH2 and RBSN is that both codes utilize the same set of nodal points, along with the natural neighbor and volume rendering definitions according to the corresponding Voronoi tessellation. Several capabilities of the linked TOUGH-RBSN simulator are validated, through simulations of: (1) pressure development with increasing saturation degree in bentonite; and (2) desiccation cracking of a mining waste. In these examples, pressure and degree of saturation supplied by TOUGH2 drive the mechanical stress and damage response of the RBSN. For the simulation of desiccation cracking, agreement between the numerical and physical test results (with respect to time to initial cracking, trends in mean crack spacing, and qualitative representation of the crack patterns) is quite good, especially when considering the strong dependence of elastic modulus and tensile strength on degree of saturation. Discrepancies in calculated observed crack spacing suggest needs for further work, including study of the effects of material toughness on desiccation cracking.

With the implemented hydro-mechanical coupling, one can simulate fractures induced by differential straining due to changes in degree of saturation, thermal contraction, and fluid overpressure. With further development, it is envisaged that the TOUGH-RBSN simulator will be an effective means for analyzing a variety of geological applications, including radioactive waste disposal, enhanced geothermal systems, petroleum recovery (*e.g.*, shale gas and oil extraction), and geologic CO_2 sequestration.

Acknowledgments

The authors gratefully acknowledge Laura Blanco Martin and Daniel Hawkes at LBNL for their careful review of a draft manuscript. The experimental data of Rodríguez *et al*. (2007) are available from ©2008 Canadian Science Publishing or its licensors and were reproduced with licensing permission from the National Research Council of Canada Research Press. Funding for this work was provided by the Used Fuel Disposition Campaign, Office of Nuclear Energy, of the U.S. Department of Energy under Contract Number DE-AC02-05CH11231 with Berkeley Lab.

References

Alonso, E.E., Alcoverro, J., *et al*., 2005. The FEBEX benchmark test: case definition and comparison of modelling approaches. International Journal of Rock Mechanics and Mining Sciences 42, 611–638.

Amarasiri, A., Kodikara, J.K., and Costa, S., 2011. Numerical modeling of desiccation cracking. Int. J. Numer. Anal. Meth. Geomech 35, 82-96.

Asahina, D. and Bolander, J.E., 2011. Voronoi-based discretizations for fracture analysis of particulate materials. Powder Technology 213, 92–99.

Asahina, D., Landis, E.N., and Bolander, J.E., 2011. Modeling of phase interfaces during pre-critical crack growth in concrete. Cement & Concrete Composites 33, 966-977.

Bastiaens W., Bernier, F., and Li, X.L., 2007. SELFRAC: Experiments and conclusions on fracturing, self-healing and self-sealing processes in clays. Physics and Chemistry of the Earth 32, 600–615.

Bear, J., 1972. Dynamics of fluids in porous media. American Elsevier Publishing Company 764 pp.

Berton, S. and Bolander, J.E., 2006. Crack band modeling of fracture in irregular lattices. Computer Methods in Applied Mechanics and Engineering, 195, 7172-7181.

Biot, M.A., and Willis, D.G., 1957. The elastic coefficients of the theory of consolidation. Journal of Applied Mechanics, 24, 594–601.

Bishop, A.W., Alpan, I., Blight, G.E., and Donald, I.B., 1960. Factors controlling the strength of partly saturated cohesive soils. Conference Shear Strength Cohesive Soils, ASCE: New York, 503–532.

Bisschop, J., 2008. Size and boundary effects on desiccation cracking in hardened cement paste. International Journal of Fracture 154, 211–224.

Bolander, J.E. and Saito, S., 1998. Fracture analyses using spring networks with random geometry. Engineering Fracture Mechanics 61, 569–91.

Bolander, J.E. and Sukumar, N., 2005. Irregular lattice model for quasistatic crack propagation. Physical Review B, 71, 094106 (12 pages).

Bossart, P., Trick, T., Meier, P.M., and Mayor, J.-C., 2004. Structural and hydrogeological characterization of the excavation-disturbed zone in the Opalinus Clay (Mont Terri Project, Switzerland). Applied Clay Science 26, 429– 448.

Chiaramonte, L., Zoback, M.D., Friedmann, J., and Stamp, V., 2008. Seal integrity and feasibility of CO_2 sequestration in the Teapot Dome EOR pilot: geomechanical site characterization. Environmental Geology 54, 1667–1675.

Colina, H. and Roux, S., 2000. Experimental model of cracking induced by drying shrinkage. European Physical Journal E 1, 189-194.

Colina, H. and Acker, P., 2000. Drying cracks: kinematics and scale laws. Materials and

Structures 33,101-107.

Cundall, P.A., 1971. A computer model for simulating progressive large scale movements in blocky rock systems. In Proceedings of the symposium of the International Society Rock Mechanics, 2,8, Nancy, France.

Cusatis, G., Bažant, Z.P., and Cedolin, L., 2003. Confinement-shear lattice model for concrete damage in tension and compression: I. Theory. Journal of Engineering Mechanics, 129 (12), 1439-1448.

Cusatis, G., Pelessone, D., and Mencarelli, A., 2011. Lattice discrete particle model (LDPM) for failure behavior of concrete. I: Theory. Cement and Concrete Composites, 33 (9), 881-890.

Dershowitz, W.S., La Pointe, P.R. and Doe, T.W., 2004. Advances in discrete fracture network modeling. Proceedings of the US EPA/NGWA Fractured Rock Conference, Portland.

Ghezzehei, T.A., Trautz, R.C., Finsterle, S., Cook, P.J., and Ahlers, C.F., 2004. Modeling coupled evaporation and seepage in ventilated cavities. Vadose Zone Journal 3:806–818.

Groisman, A. and Kaplan, E., 1994. An experimental study of cracking induced by desiccation. Europhysics letters 25:415–420.

Herrmann H.J., Roux S., 1990. Statistical models for the fracture of disordered media. The Netherlands: Elsevier/North Holland, Amsterdam.

Itasca Consulting Group, 2009. FLAC^{3D}, fast Lagrangian analysis of continua in 3 dimensions (ver. 4.0). Minneapolis, Minnesota: Itasca Consulting Group; p. 438.

Jing, L, and Hudson, J.A., 2002. Numerical methods in rock mechanics. International Journal of Rock Mechanics and Mining Sciences 39, 409–427.

Kawai, T., 1978. New discrete models and their application to seismic response analysis of structures. Nuclear Engineering and Design 48, 207-229.

Kim J., and Moridis G. J., 2013. Development of the T+M coupled flow-geomechanical simulator to describe fracture propagation and coupled flow-thermal-geomechanical processes in tight/shale gas systems. (submitted for publication)

Kitsunezaki, S., 2011. Crack growth in drying paste. Advanced Powder Technology 22, 311–318.

Konrad, J.-M. and Ayad, R., 1997. Desiccation of a sensitive clay: field experimental observations. Canadian Geotechnical Journal, 34: 929–942.

Lakshmikantha, M.R., Prat, P.C., and Ledesma, A., 2012. Experimental evidence of size effect in soil cracking. Canadian Geotechnical Journal 49, 264–284.

Nagai, K., Sato, Y., and Ueda, T., 2005. Mesoscopic simulation of failure of mortar and concrete by 3D RBSM. Journal of Advanced Concrete Technology 3(3), 385-402.

Neuzil, C.E., 2003. Hydromechanical coupling in geologic processes. Hydrogeology Journal 11, 41–83.

Noorishad, J., Ayatollahi, M.S., and Witherspoon, P.A., 1982. A finite-element method for coupled stress and fluid flow analysis in fractured rock masses. International Journal of Rock Mechanics and Mining Sciences & Geomechanics Abstracts 19, 185–193.

Okabe, A., Boots, B., Sugihara, K., and Chiu, S.N., 2000. Spatial Tessellations: Concepts and

Applications of Voronoi Diagrams (Second Edition). Wiley Series in Probability and Mathematical Statistics, John Wiley & Sons Ltd., England.

Oldenburg, C.M. and Pruess, K., 1995. EOS7R: Radionuclide Transport for TOUGH2. Lawrence Berkeley National Laboratory, LBL-34868.

Paluszny, A., Matthai, S.K., and Hohmeyer, M., 2007. Hybrid finite element–finite volume discretization of complex geologic structures and a new simulation workflow demonstrated on fractured rocks. Geofluids 7, 186–208.

Pan, P.-Z., Yan, F., and Feng, X.-T., 2012. Modeling the cracking process of rocks from continuity to discontinuity using a cellular automaton. Computers & Geosciences 42, 87-99.

Painter, S. and Cvetkovic, V., 2005. Upscaling discrete fracture network simulations: An alternative to continuum transport models. Water Resources Research, 41, 2.

Pruess, K., Oldenburg, C., and Moridis, G., 2011. TOUGH2 User's Guide, Version 2. Lawrence Berkeley National Laboratory, LBNL-43134 (revised).

Reichenberger, V., Jakobs, H., Bastian, P., and Helmig, R., 2006. A mixed-dimensional finite volume method for two-phase flow in fractured porous media. Advances in Water Resources 29, 1020–1036.

Rodríguez, R. Sánchez, M., Ledesma, A., and Lloret, A., 2007. Experimental and numerical analysis of desiccation of a mining waste. Canadian Geotechnical Journal, 44, 644-658.

Rutqvist, J., Börgesson, L., Chijimatsu, M., Kobayashi, A., Jing, L., Nguyen, T.S., Noorishad, J., and Tsang, C.-F., 2001. Thermohydromechanics of partially saturated geological media:

governing equations and formulation of four finite element models. International Journal of Rock Mechanicas & Mining Sciences 38, 105-127.

Rutqvist, J., Ijiri, Y., and Yamamoto, H., 2011. Implementation of the Barcelona Basic Model into TOUGH–FLAC for simulations of the geomechanical behavior of unsaturated soils. Computers & Geosciences 37, 751–762.

Rutqvist, J., and Stephansson, O., 2003. The role of hydromechanical coupling in fractured rock engineering. Hydrogeology Journal, 11, 7–40.

Rutqvist, J., Leung, C., Hoch, A., Wang, Y., Wang, Z., 2013. Linked multicontinuum and crack tensor approach for modeling of coupled geomechanics, fluid flow and transport in fractured rock. Journal of Rock Mechanics and Geotechnical Engineering 5, 18-31.

Rutqvist, J., and Tsang, C.-F., 2002. A study of caprock hydromechanical changes associated with CO_2-injection into a brine formation. Environmental Geology, 42, 296-305.

Rutqvist, J., Wu, Y.-S., Tsang, C.-F., and Bodvarsson, G., 2002. A modeling approach for analysis of coupled multiphase fluid flow, heat transfer, and deformation in fractured porous rock. International Journal of Rock Mechanics & Mining Sciences, 39, 429–442.

Shin, H. and Santamarina, J.C., 2011. Desiccation cracks in saturated fine-grained soils: particle-level phenomena and effective-stress analysis. Géotechnique 61,961–972.

Shen, B., Stephansson, O., Rinne, M., Lee, H.-S., Jing, L., and Röshoff, K., 2004. A fracture propagation code and its applications to nuclear waste disposal. International Journal of Rock Mechanics and Mining Sciences & Geomechanics Abstract 41, 448-449.

Shorlin, K.A., de Bruyn, J.R., Graham, M., and Morris, S.W., 2000. Development and geometry of isotropic and directional shrinkage crack patterns. Physical Review E, 61,6950-6957.

Sukumar, N. and Bolander, J.E., 2013. Voronoi-based interpolants for fracture modeling. In van de Weygaert R., Vegter G., Ritzerveld J., Icke V., editors. Tessellations in the Sciences; Virtues, Techniques and Applications of Geometric Tilings. Springer Verlag (to appear).

Tang, C.A., Tham, L.G., Lee, P.K.K., Yang, T.H., and Li, L.C., 2002. Coupled analysis of flow, stress and damage (FSD) in rock failure. International Journal of Rock Mechanics & Mining Sciences 39, 477–489.

Trabelsi, H., Jamei, M., Zenzri, H., and Olivella, S., 2011. Crack patterns in clayey soils: Experiments and modeling. Int. J. Numer. Anal. Meth. Geomech 36, 1410-1433.

Vilarrasa, V., Bolster, D., Olivella, S., and Carrera, J., 2010. Coupled hydromechanical modeling of CO2 sequestration in deep saline aquifers. Int. J. Greenhouse Gas Control 4, 910-919.

van Genuchten, M.T., 1980. A closed-form equation for predicting the hydraulic conductivity of unsaturated soils. Soil Science Society of America Journal, 44, 892-898.

van Mier J.G.M., 1997. Fracture processes of concrete: assessment of material parameters for fracture models, new directions in civil engineering. Boca Raton: CRC Press.

van Vliet, M.R.A. and van Mier, J.G.M., 1999. Effect of strain gradients on the size effect of concrete in uniaxial tension. International Journal of Fracture 95,195-219.

Yip, M., Li, Z., Liao, B.-S., and Bolander, J.E., 2006. Irregular lattice models of fracture of multiphase particulate materials. International Journal of Fracture 140,113–124.

Zhang, K., Wu, Y.S., Bodvarsson, G.S., and Liu, H.H., 2004. Flow focusing in unsaturated fracture networks: A numerical investigation, Vadose Zone Journal 3,624-633.

LIST OF FIGURE

Fig. 8. Evolution of gravimetric moisture content of sample with thickness of 16mm.

Fig. 9. Voronoi discretization of the mining waste sample with 16 mm thickness.

Fig. 10. Dependence of crack patterns on nodal density for sample thicknesses of: (a), (b) 8 mm; and (c), (d) 16 mm.

Fig. 11. Crack patterns for different sample thicknesses: (a) experimental results of Rodríguez *et al*. (2007), and (b) plan view of 3-D simulation results of the TOUGH-RBSN simulator.

Fig. 12. Variation of mean spacing of cracks with sample thickness. The additional test results are also taken from Rodríguez *et al*. (2007), but for different drying conditions.

LIST OF TABLES